Korean J. Chem. Eng., 39(5), 1146-1157 (2022)
DOI: 10.1007/s11814-021-1008-9

pISSN: 0256-1115
eISSN: 1975-7220

Effect of baffle configuration on performance of batch stirred vessel

Basheer Ashraf Ali† and Lister Herington Falleiro

Department of Chemical Engineering, NITK Surathkal, Mangalore, Karnataka 575025, India
(*Received 12 June 2021 • Revised 4 November 2021 • Accepted 8 November 2021*)

Abstract−Crystallization is often carried out in batch stirred vessels. However, it is difficult to obtain uniform crystal size distribution (CSD), as it strongly depends on prevailing flow field operating conditions. This is adversely affected by the geometry of stirred vessels. Hence in this work, CFD simulations were performed to investigate flow field, mixing and crystallization phenomena in a stirred vessel. The performance of the stirred vessel was compared with draft tube baffled stirred vessel. The flow field was quantified through liquid circulation and vorticity. The mixing was analyzed through macromixing time in the stirred vessel. The solubility data, nucleation, and growth kinetics were integrated with CFD through a user-defined function (UDF) to predict crystallization phenomena. The predicted results were validated with experimental data available in the literature. The effects of seed mass, size and temperature on CSD were investigated and optimum conditions [750 gm (seed mass); 500 μm (seed size); 308 K (temperature)] for favourable crystal growth were identified. The performance of the proposed baffled stirred vessel was found to be significant, and it supports enhancing flow field, mixing and crystallization process.

Keywords: Hydrodynamics, Mixing, Crystal Growth, Nucleation, CFD, Population Balance Model

INTRODUCTION

Stirred vessels are simple in design, in which impellers are used for the generation of flow field and mixing. In such systems, the heat and mass transfer characteristics are significant [1]. Hence, they are widely used in chemical, biochemical, petrochemical and allied industries, such as batch processing of emulsions, crystallization and pharmaceutical applications [2,3].

However, due to the complex hydrodynamics of fluid phase mixing in such stirred vessels, numerous challenging problems still exist for improving the flow field and quality of mixing [4]. The performance of stirred vessels is mainly influenced by the aspect ratio type of location of the impeller, shape of the reactor and configuration of the baffle [5]. The proper stirred vessel configuration is necessary to reduce inhomogeneity and to achieve the desired flow characteristics [6]. The impeller blades modify the flow field, mixing and reducing the power consumption in stirred vessels [7]. The swirling strength increases with the increase in the turbulence level in the stirred vessel [8]. The turbulence levels in the stirred vessel are improved by the appropriate design of the baffles [9]. Once a proper stirred vessel configuration is identified, it is used for industrial applications such as pharmaceuticals, catalytic, crystallization, sterilization and mineral industries.

Computational fluid dynamics (CFD) has been widely used to design suitable stirred vessel configurations [10]. The fluid phase mixing in stirred vessels reduces inhomogeneity present in the system, for example, reducing the non-uniformity of particle distributions in particle-liquid systems. The particle-liquid suspension is improved by choosing an appropriate impeller design [11]. Further, a suitable baffle configuration improves the flow distribution and mixing of particles in stirred vessels [12]. Wang et al. [13] introduced a draft tube in the stirred vessel and found that it influences the particle dispersion at lower impeller speeds. The flow field in a stirred vessel has been modelled using several approaches [14,15]. Ali and Solsvik [3] found that mass transfer in stirred vessel systems is significant when inviscid fluids are used. The presence of primary and secondary circulation flows with small scale eddies affects the performance of stirred vessels [16].

A batch stirred vessel system can carry out the crystallization process and obtain pure crystalline materials with a controlled size range and shape [17]. These characteristics of the crystal control the downstream processing steps such as filtration and drying [18]. The quality of crystals strongly depends on various operating conditions in a crystallizer such as local supersaturation, hydrodynamics, fluid mixing, geometry, modes of crystallizer operation, seeding, aggregation, breakage and hence the crystal size distribution (CSD) [19,20].

Since the dependence of growth and nucleation rates on supersaturation is highly system-specific, determining the optimum conditions that produce the desired crystalline product requires numerous bench-scale experiments [21]. These conditions might not be optimal after the scale-up of the crystallizer as the liquid phase mixing influences the local supersaturation [6,22]. This motivates us to use the CFD to predict the crystallization process and quantify the effects of flow-induced mixing on crystal size distribution (CSD).

The desired CSD can be obtained by controlled seed characteristics such as mass, size distribution, time for adding the seed crystals and seed temperature [23]. These factors significantly influence final CSD and hence product quality [24]. The optimum characteristics of seed crystal suppress spontaneous nucleation and support crystal growth. Doki et al. [25] proposed an empirical cor-

†To whom correspondence should be addressed.
E-mail: ashrafali@nitk.ac.in

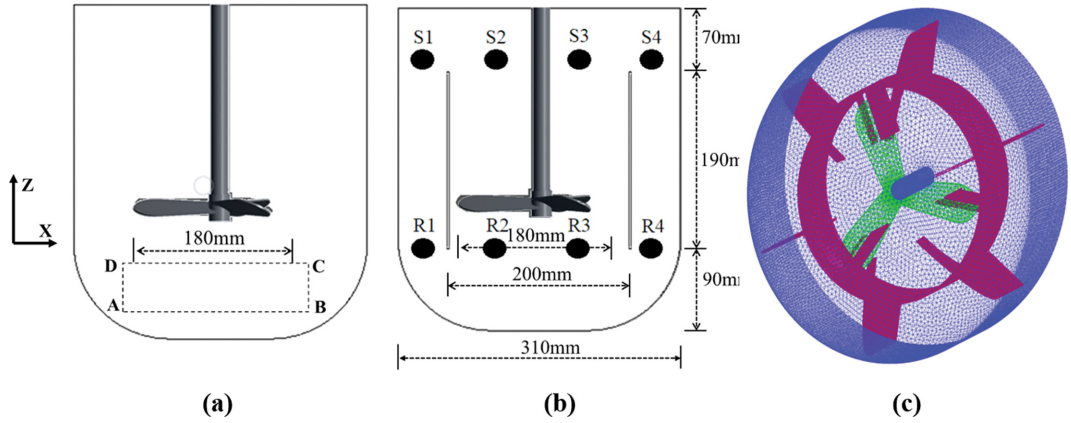

Fig. 1. Schematic of the (a) unbaffled, (b) baffled, (c) 3D mesh (baffled) stirred vessel system.

relation to estimate the critical seed mass (Cs*). Due to higher contact probability and contact energy, large seed crystals generate more secondary nuclei than small seeds [26]. Hence, optimum seeding conditions are needed [23] to improve poorly behaved crystals in a batch stirred vessel. Doki et al. [27] found a uni-modal CSD when the seed loading was above critical seed concentration and a bimodal CSD below a crucial seed concentration. Wei et al. [28] characterized supersaturation distribution in a 3D batch crystallizer. They found that the liquid phase mixing and CSD are influenced by impeller speed and feed injection location. Wang et al. [29] studied the effect of feed location, feed concentration, and impeller speed on barium sulfate residence time precipitate in a stirred tank crystallizer using CFD. Trampuž et al. [30] found that the CSD depends on the impeller speed, cooling rate and the seeding strategy in the batch crystallizer.

The energy dissipation rate is high in a stirred vessel due to significant local gradients [31]. Here, various impellers and baffles are used to produce different flow patterns and mix [32]. The hydrodynamics of a given system influences scale-up of the crystallization process. Hence, finding an optimum configuration of the stirred vessel is crucial that supports the desired CSD. In our earlier work on the same batch stirred vessel [33], the liquid volume of 24 L was more advantageous for the crystallization process.

Further, Temmel et al. [34] experimentally found optimum kinetic parameters by considering KH_2PO_4 crystals in water in the same system (24 L) crystallizer. Lewis et al. [35] predicted CSD using known kinetic models by integrating the population balance equation (PBE) [36] into the CFD solver. But the spatial inhomogeneity in the temperature, solute supersaturation and particle concentration is not considered in their computational methodology.

Hence, in the present investigation, hydrodynamic and mixing in an unbaffled stirred vessel are improved by introducing the draft tube baffle configuration. The optimum stirred vessel is identified that supports the desired CSD, nucleation and growth rates of KH_2PO_4 crystals, where solubility, crystal growth and nucleation kinetics are used. Here coupled CFD-PBE methodology is used to predict the motion of crystals in the batch stirred vessel. The effect of seed crystal mass, seed crystal size and temperature on CSD was investigated, and optimum conditions were found.

The manuscript is organized by discussing the geometry of batch crystallizers in section 2.1. Then, the transport equations and simulation methodology are described in sections 2.2 and 2.3. In section 3, numerical predictions are discussed and, finally, key findings are summarized in section 4.

COMPUTATIONAL METHODOLOGY

1. Geometry

The schematics of the unbaffled and baffled crystallizers are shown in Fig. 1(a) and 1(b). The stirred vessel has an inner diameter of 310 mm and 350 mm in height. A propeller type impeller (axial) of 180 mm diameter with the blades pitched horizontally at an angle of 30° is used. The impeller is placed at the height of 120 mm from the bottom of the stirred vessel.

The baffled vessel has a draft tube baffle of 200 mm diameter and a height of 190 mm, placed at 90 mm from the bottom of the vessel. The draft tube has three inner baffles, each with a width of 50 mm and arranged at an angle of 120°. The draft tube has six outer baffles, each having a width of 50 mm and positioned at an angle of 60°. The computational grid used for the 3D baffled stirred vessel is shown in Fig. 1(c).

2. Transport Equations

The flow field in the stirred vessel was numerically investigated, assuming the liquid temperature to be at 298 K. The Reynolds number is calculated using [33,37]

$$\mathrm{Re}=\frac{\mathrm{ND}^2\rho}{\mu} \tag{1}$$

Here, N is the impeller rotational speed (rps), D is the diameter (m) of the impeller, ρ is the density (kg/m^3), and μ are the viscosity (Pa·s) of the liquid. The Reynolds number for 300 rpm is found to be 202,500. Hence, the standard k-ε turbulence model is used to predict liquid-phase turbulence in the batch stirred vessel.

The conservation equation for continuity and momentum are

$$\underbrace{\frac{\partial}{\partial t}(\alpha_q\rho_q)}_{\text{Transient}}+\underbrace{\nabla\cdot(\alpha_q\rho_q\vec{v}_q)}_{\text{Convective}}=\underbrace{\Sigma_{p=1}^{n_p}\dot{m}_{pq}}_{\text{interphase mass exchange}} \tag{2}$$

where α, ρ, $\vec{v}_q$ are the volume fraction, density, and velocity of the q phase, respectively.

$$\underbrace{\frac{\partial}{\partial t}(\alpha_q\rho_q\vec{V}_q)}_{Transient} + \underbrace{\nabla\cdot(\alpha_q\rho_q\vec{V}_q\vec{V}_q)}_{Convective} = \underbrace{-\alpha_q\nabla p}_{Pressure} - \underbrace{\nabla\cdot\bar{\bar{\tau}}_q}_{shear} + \underbrace{\alpha_q\rho_q g}_{body}$$
$$+\Sigma\left(\underbrace{R_{pq}}_{\substack{interphase\ force\\ exchange}} + \underbrace{\dot{m}_{pq}\vec{V}_q}_{\substack{interphase\ force\\ exchange}}\right) + \underbrace{\alpha_q\rho_q F_{td,\,q}}_{Drag\ force} \quad (3)$$

where P is particle pressure, $R_{ls}$is the interaction force, $\vec{V}_{ls}$ is the interphase velocity. The second term on the RHS of Eq. (3) represents momentum flux $\bar{\bar{\tau}}$ due to particle stress-strain tensor, third term is the body force term, and fourth term accounts for interaction force between the two phases.

The interphase force exchange term is modelled using phase velocities,

$$R_{ls} = K_{ls}(\vec{V}_l - \vec{V}_s) \quad (4)$$

where, K_{ls} is the interphase momentum exchange coefficient that depends on drag function and particle relaxation time. The drag model given by Ding and Gidaspow [38] is used to predict the interphase momentum exchange (K_{ls}).

The dispersed k-ε turbulence model is used to predict liquid phase turbulence:

$$\frac{\partial}{\partial t}(\alpha_l k_l) + \nabla\cdot(\vec{V}_l\alpha_l k_l) = \nabla\cdot\left(\alpha_l\left(\mu_l + \frac{\mu_{t,l}}{\sigma_k}\right)\nabla k_l\right) + \alpha_l G_{k,\,l} + -\alpha_l\varepsilon + \alpha_l\pi_{kl} \quad (5)$$

$$\frac{\partial}{\partial t}(\alpha_l\varepsilon_l) + \nabla\cdot(\vec{V}_l\alpha_l\varepsilon_l) = \nabla\cdot\left(\alpha_l\left(\mu_l + \frac{\mu_{t,l}}{\sigma_\varepsilon}\right)\nabla\varepsilon_l\right) + \alpha_l\frac{\varepsilon_l}{k_l}(C_{1\varepsilon}G_{k,\,l} - C_{2\varepsilon}\varepsilon_l) + \alpha_l\pi_{\varepsilon l} \quad (6)$$

where $G_{k,l}$ is the turbulence kinetic energy production due to mean velocity.

The crystal size distribution in our stirred vessel is predicted using population balance equations (PBE). The PBE is described using the number density function (NDF), and it is given (particle volume, V) by

$$\frac{\partial}{\partial t}[n(V,t)] + \nabla\cdot[\vec{u}n(V,t)] + \nabla_V\cdot\underbrace{[G_V n(V,t)]}_{Growth\ term} =$$
$$\underbrace{\frac{1}{2}\int_0^V a(V-V',V')n(V-V',t)n(V',t)dV'}_{Birth\ due\ to\ Aggregation} -$$
$$\underbrace{\int_0^\infty a(V,V')n(V,t)n(V',t)dV'}_{Death\ due\ to\ Aggregation} +$$
$$\underbrace{\int_{\Omega v} p\ g(V')\beta(V|V')n(V')dV'}_{Birth\ due\ to\ Breakage} - \underbrace{g(V)(V,t)}_{Death\ due\ to\ breakage} \quad (7)$$

Here n represents the number density of particles of volume V at time t. The initial and boundary conditions are

$$n(V,t=0) = n_V;\ n(V=0,t)\ G_v = B \quad (8)$$

where, n(V, t) is number density function, G_v is the growth rate based on the volume of the particle, n_V is the initial number density of the seed crystals, B is the nucleation rate (#/m^3·s). Since the magnitude of agglomeration is insignificant for crystal size greater than 50 μm [39], crystal breakup and agglomeration are not considered in the present work. Thus, Eq. (7) becomes,

$$\frac{\partial}{\partial t}[n(V,t)] + \nabla\cdot[\vec{u}n(V,t)] + \nabla_V\cdot\underbrace{[G_V n(V,t)]}_{Growth\ term} = 0 \quad (9)$$

The single particle volume (V) is given by

$$V = k_v L^3 \quad (10)$$

The relationship between G_v and G (growth) is

$$G_v = 3k_v L^2 G \quad (11)$$

The volumetric shape factor (k_v) for KH_2PO_4 crystal is 0.75. The growth (G) and nucleation (B) kinetics for KH_2PO_4 - water system is implemented using a user-defined function (UDF) in CFD commercial software package (ANSYS Fluent 2020 R2). The solubility data, nucleation and growth kinetics for KH_2PO_4 crystals are

$$B = 5.2\times10^{-2}e^{\left(\frac{-1,000}{RT}\right)}(S-1)^{5.8} \quad (12)$$

$$G = 5.1\times10^{6}e^{\left(\frac{-70,000}{RT}\right)}(S-1)^{1.26} \quad (13)$$

$$S = c(t)/c^*(\theta) \quad (14)$$

$$c^*(\theta) = 15.24 + 0.206\theta + 1.01\times10^{-2}\theta^2 - 1.45\times10^{-4}\theta^3 + 1.23\times10^{-6}\theta^4 \quad (15)$$

where B (#/m^3·s) is the nucleation rate, R (J/mol·K) is the universal gas constant, T (K) is the solution mixture temperature, G (m/s) is the growth rate of the crystals, S is the relative supersaturation, $c^*(\theta)$ saturation concentration of KH_2PO_4 at the temperature (^{o}C), and c(t) is the concentration of the KH_2PO_4 solute at time instant (s). The crystallization kinetics [(12) and (13)] are valid when the solution is supersaturated (i.e., S>1).

The PBEs are solved using the quadrature method of moments (QMOM) [40]. The quadrature approximation is based on determining a sequence of polynomials orthogonal to the particle size distribution n (L).

$$\mu_k = \int_0^\infty f(L)n(L)dL = \int_0^\infty n(V,t)L^k dL \approx \Sigma_{i=1}^N f(L_i)\omega_i \quad (16)$$

where ω_i is the weights and L_i is the abscissas that are determined using the product difference (PD) algorithm from the lower order moments. The "N" is the order of approximation, and k is the specified number of moments used to solve the PBE. Eq. (9) is transformed using Eq. (16). The initial moment's distribution is obtained using [41].

$$\mu_i^s = N_s L_s^i \quad (17)$$

where, μ_i^s is the i^{th} moment with i=0, 1, 2, …5; L_s is the size of the seeded crystals, N_s is the number of seed crystals, and it is calculated by

$$N_s = \frac{M_s}{\rho_c k_v L_s^3} \quad (18)$$

where M_s is the mass of the seed crystals introduced in our stirred vessel, k_v is the volume shape factor, ρ_c is the density of KH_2PO_4 (2,340 kg/m^3). The moments obtained at the end of the flow simulation time are reconstructed to obtain crystal size distribution (CSD) [42]. The PBE is coupled with Euler - Granular model through the Sauter mean diameter ($d_{32}=\mu_3/\mu_2$) to calculate the interfacial properties, namely, drag force. The third-order moment (μ_3) is related to the volume fraction of the dispersed (particle) phase is,

$$\alpha_s = k_V \Sigma_{q=1}^{N} \omega_q L_q^3 \tag{19}$$

The sum of volume fraction of continuous (liquid) and dispersed (particle) phase is considered to be unity:

$$\Sigma_{q=1}^{n_p} \alpha_q = 1 \tag{20}$$

3. Simulation Methodology

The flow field, mixing, and CSD in a batch stirred vessel are predicted using commercial CFD software (ANSYS Fluent 2020 R2). The ANSYS design modeller is used to develop the geometry of the stirred vessel, and ICEM CFD is used for meshing. CFD simulations are checked for three different grids 500000, 750000 and 1000000. To ensure grid-independence of CFD predictions, spatial variation of the predicted velocity magnitude is compared for different grids, and optimum grid size (750000) is determined. The liquid phase turbulence in stirred vessel system is predicted using the standard k-ε model. The multiple reference frame (MRF) and sliding mesh (SM) approaches are used to predict the flow field. Once the flow field is converged, a pulse of the tracer is introduced at the top of the vessel. The concentration of the tracer is monitored at eight different locations. The time taken for the concentration of the tracer to reach 95% uniformity is considered to be the mixing time for the stirred vessel system.

To predict the crystal size distribution, the KH_2PO_4 - water system is considered. CFD simulations are performed using QMOM to discretize the PBE. The growth and nucleation rate are defined through a UDF to account for the equilibrium solubility, temperature, and solute concentration. The UDF uses the physical properties of dissolved KH_2PO_4 in H_2O. The UDF first calculates the equilibrium solubility using Eq. (15). This depends on the solution temperature. The calculated solubility of KH_2PO_4 in water is used in Eq. (14), and supersaturation is computed by considering the mass fraction of KH_2PO_4. The nucleation and growth rate are predicted through Eqs. (12) and (13), respectively, incorporating solution temperature and supersaturation data at every computational cell. The CFD simulation is initialized with a KH_2PO_4 mass fraction of 0.32, solution temperature of 308 K and relative supersaturation at 1.05. The walls of the stirred vessel are maintained at 298 K.

The crystal size distribution (CSD) is reconstructed from the finite set of moments [42] obtained by solving full PBEs. The first six moments are used to reconstruct the CSD using the cubic spline-based method [42] through piecewise polynomial function.

The baffles and tank walls are specified as a no-slip boundary condition (BC). The impeller is modelled as no-slip BC with zero relative velocity. The top liquid level of the stirred vessel is modelled as a horizontal surface where slip condition is imposed. Here, transient CFD simulations are performed with an adaptive time step (Δt- 10 μs - 10 ms). The convergence criterion for residuals is set to be 10^{-6} for all the transport variables.

RESULTS AND DISCUSSION

1. Flow Field

At first, the flow field in a batch stirred vessel is investigated for an impeller speed of 300 rpm. To characterize the flow field, a vertical plane at y=−0.005 m is chosen. The predicted contours of velocity magnitude are analyzed for unbaffled and baffled stirred vessels (Fig. 2).

It is observed that the velocity magnitude is higher near the impeller in both the unbaffled and baffled systems. As impeller blades are pitched at an angle of 30 degrees, the liquid is pushed downwards and then forced to move upwards along the vertical vessel

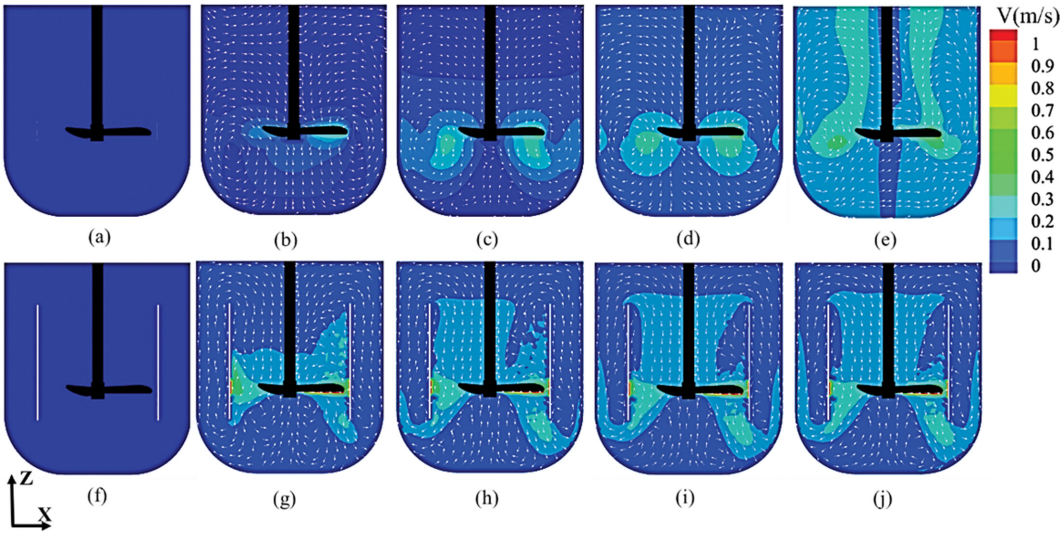

Fig. 2. Contours of normalized velocity magnitude at different time instants 0 s, 0.2 s, 0.6 s, 1 s and 5 s for the unbaffled (top row) and baffled (bottom row) stirred vessel.

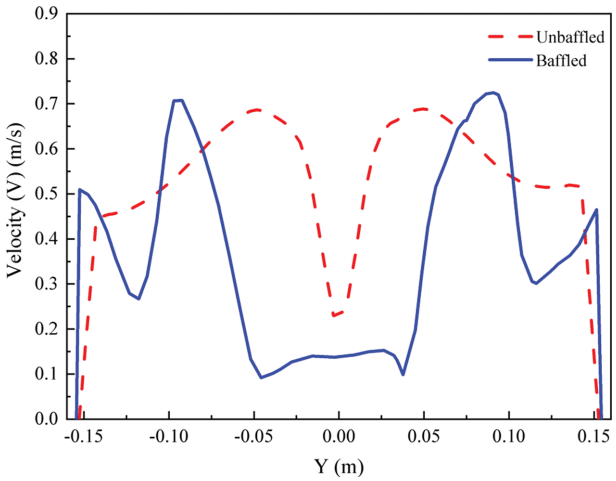

Fig. 3. Spatial variation of velocity magnitude (m/s) along a horizontal line z=−0.005 m when flow time is 60 s.

walls. The secondary recirculation in the flow field is observed to be weak in the unbaffled stirred vessel system and strong in the baffled stirred vessel.

To quantify the flow field, a horizontal line (z=−0.01 m) is chosen below the impeller, and spatial variation of velocity magnitude across the line is analyzed (Fig. 3).

It is observed that the velocity magnitude is zero close to the wall and maximum near the impeller. As the impeller speed (300 rpm) in both unbaffled and baffled systems is the same, the observed order of magnitude in the velocity is identical for both systems. The nature of the predicted velocity magnitude is attributed to weak recirculation zones below the impeller.

To find an optimum impeller rotational speed in stirred vessel system, the irreversibility induced by the impeller is quantified (liquid circulation). This is calculated by taking the line integral of velocity over a closed region [43] using

$$\Gamma=\oint \mathrm{u}\cdot \mathrm{d}l \tag{21}$$

where 'dl' is the small differential element of the closed curve in the flow domain and "u" is the normal liquid velocity. The calculation domain for liquid circulation ABCD is shown in Fig. 1(a), and the line integral of fluid velocity along the closed curve is calculated to obtain the magnitude of liquid circulation.

The liquid circulation is calculated for the various rotational speeds of the impeller. The performance of the unbaffled system is compared with a baffled system [Fig. 4(a)]. The calculated liquid circulation in the baffled system is found to be one order of magnitude higher than the unbaffled system at 300 rpm. The maximum value of liquid circulation is observed when 300 rpm is used and, hence, it is considered to be optimum. Further, to verify this optimum impeller speed, the volume-weighted average of vorticity magnitude is analyzed for baffled and unbaffled systems [Fig. 4(b)]. The vorticity magnitude is observed to increase with an increase in rotational motion of the impeller, and its value is high when a baffled system is used. The vorticity magnitude is found to be maximum at 300 rpm. Once again, it confirms the earlier finding of optimum impeller motion (300 rpm).

2. Macromixing

To characterize macro mixing in the stirred vessel system, a pulse of tracer (c=55.4 kmol/L) is injected at time t=0 s. To quantify the macro-mixing time in the system, eight different point locations (Fig. 1(a)) are chosen so that four injection locations are above the impeller and the rest are below the impeller. The concentration of tracer is monitored with time at 300 rpm, and it is shown in Fig. 5(a). It is observed that the average concentration of tracer reaches a steady-state value (10 s) after initial transient fluctuations. Here, the time taken for the concentration of tracer to reach 95% of the final concentration is considered to be the macro mixing time [44]. The mixing time is calculated for various impeller speeds (50 to 350 rpm) for unbaffled and baffled stirred vessels, and it is depicted in Fig. 5(b).

The magnitude of mixing time is observed to be smaller for baffled and larger for an unbaffled stirred vessel system. This is attributed to the significant exchange of mass, momentum between the inner (rotating) and outer (stagnant) domain in baffled stirred

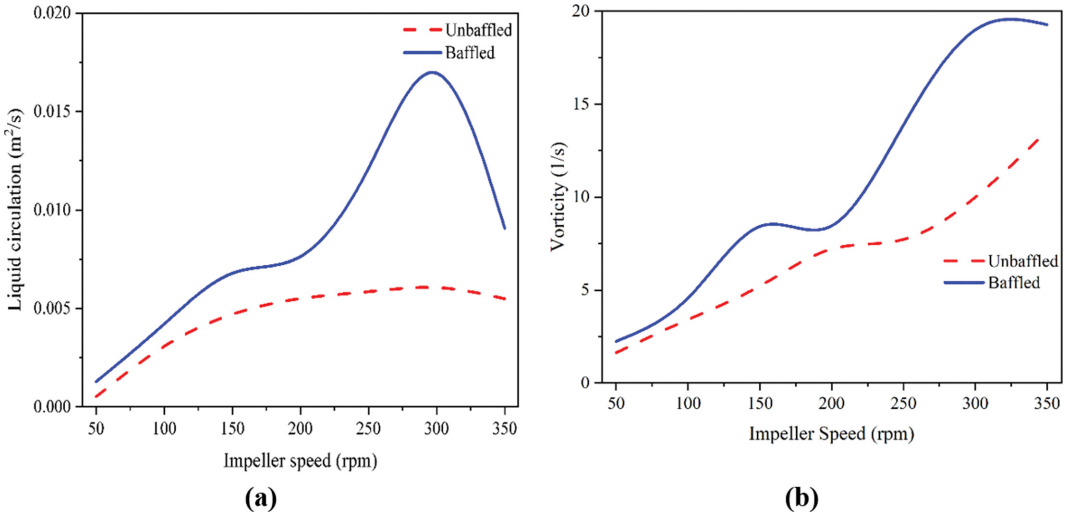

Fig. 4. Effect of impeller speed on the (a) liquid circulation and (b) vorticity when flow time is 60 s.

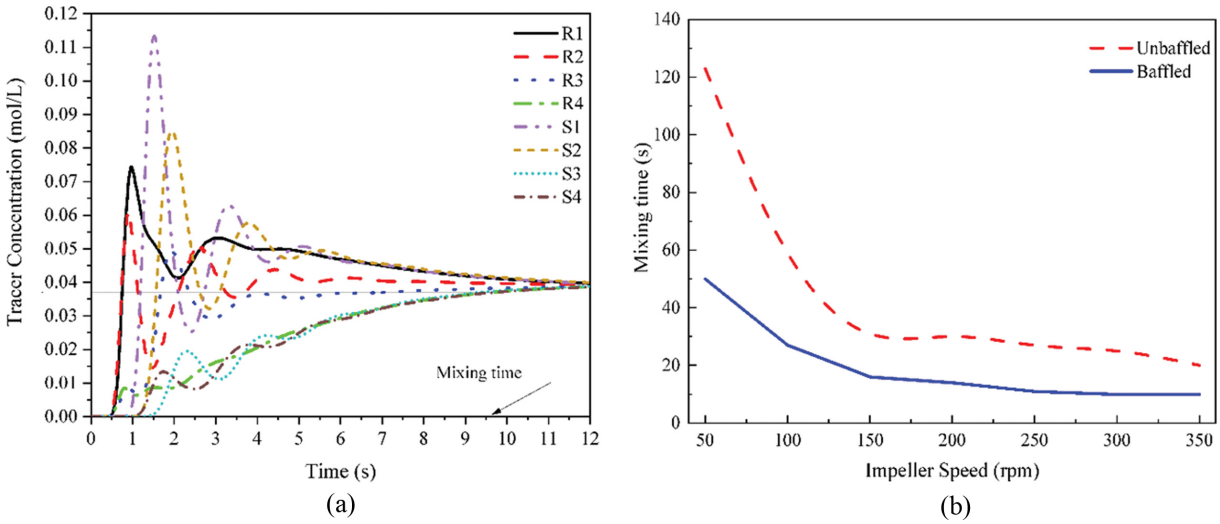

Fig. 5. (a) Evolution of tracer concentration with time (b) Effect of impeller speed on mixing time.

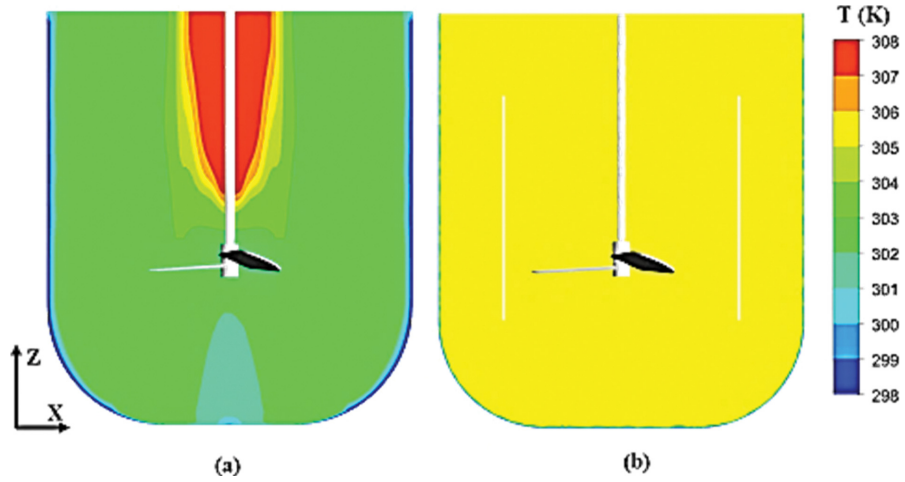

Fig. 6. Contours of temperature distribution (a) unbaffled and (b) baffled stirred vessel at the end of 60 s.

vessel configuration. Mixing time is found to be constant beyond 300 rpm. This is due to the extent of the convective flow pattern at the higher rotational motion of the impeller. Hence, the impeller speed of 300 rpm is considered optimum.

To further analyze the macro mixing characteristics, the water in the stirred vessel is cooled from 308 K by maintaining the walls at a fixed temperature of 298 K. The predicted contours of temperature distribution (y=−0.005 m) for unbaffled and baffled configuration are shown in Fig. 6. It is observed that the temperature distribution is uniform in the baffled stirred vessel system and non-uniform in the unbaffled system. To quantify this, a horizontal line is chosen at z=−0.005 m, and the spatial variation of temperature of the water is analyzed. This is shown in Fig. 7.

It is observed that the temperature is uniform (305 K) for baffled and non-uniform for unbaffled stirred vessel system. This is attributed to weak secondary recirculation in the unbaffled stirred vessel. Thus, the baffled configuration (better thermal homogeneity) is found to be more advantageous to carry out the crystallization of KDP.

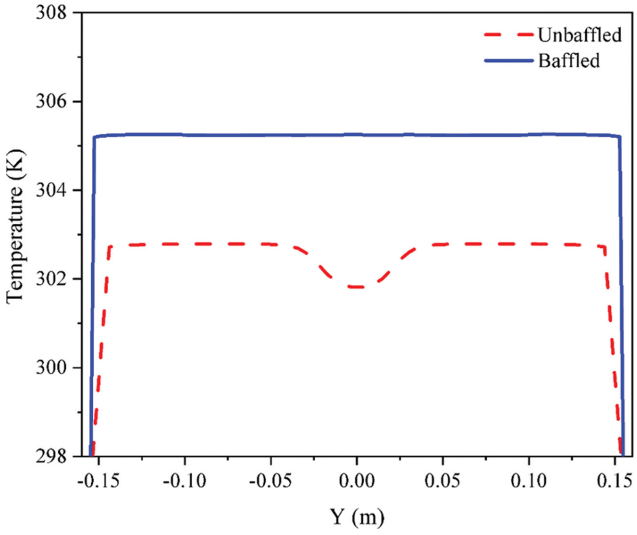

Fig. 7. Spatial variation of water temperature along z=−0.005 m at the end of 60 s.

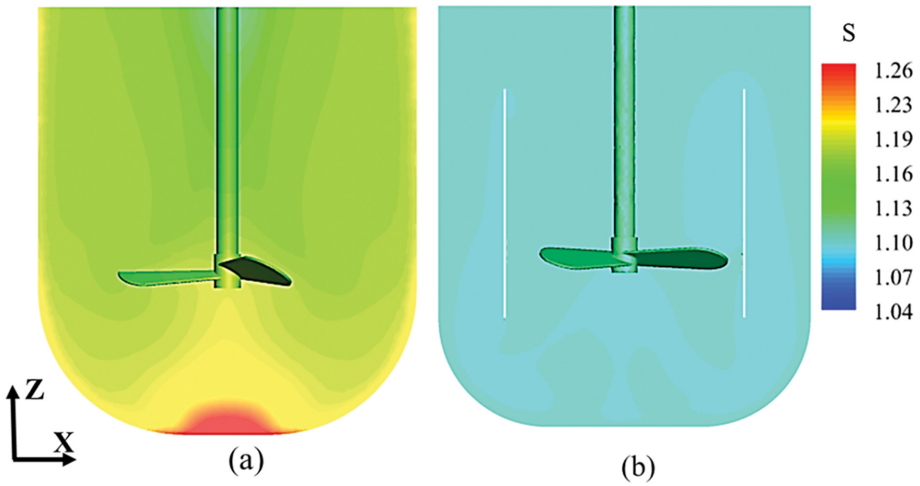

Fig. 8. Contours of supersaturation (a) unbaffled and (b) baffled stirred vessel when flow time is 60 s.

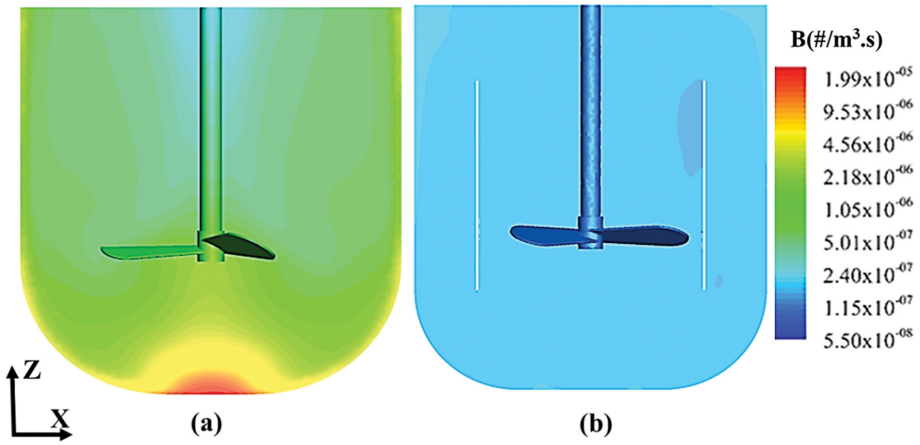

Fig. 9. Contours of nucleation rate (a) unbaffled and (b) baffled stirred vessel when flow time is 60 s.

3. Crystallization

Further, the nucleation and growth of KDP crystals in the stirred vessel are investigated. This is modelled using QMOM through the population balance model (PBM). The initial temperature of the supersaturated solution is considered to be 308 K, and the walls of the stirred vessel are cooled to 298 K. As the temperature of water decreases due to cooling, the solubility of KH_2PO_4 decreases and hence its supersaturation increases. The local supersaturation is calculated using a UDF. As supersaturation influences the nucleation and crystal growth rate in the stirred vessel system, it is analyzed for unbaffled and baffled stirred vessels. The predicted contours of local supersaturation (y=−0.005 m) when flow time is 60 s are shown in Fig. 8.

It is observed that the magnitude of supersaturation is found to be uniform in the baffled and non-uniform in the unbaffled stirred vessel system. This is attributed to the significant extent of mixing among the fluid elements in the baffled stirred vessel. Supersaturation is a function of solubility that depends on the solution temperature Eq. (14). It is observed in Fig. 7 that the temperature is lower in the region below the impeller in the unbaffled stirred vessel. A comparatively low temperature indicates lower solubility and higher supersaturation. Hence it is observed in Fig. 8 that the supersaturation is comparatively higher (red color) in the unbaffled stirred vessel. These predictions once again support a baffled stirred vessel configuration.

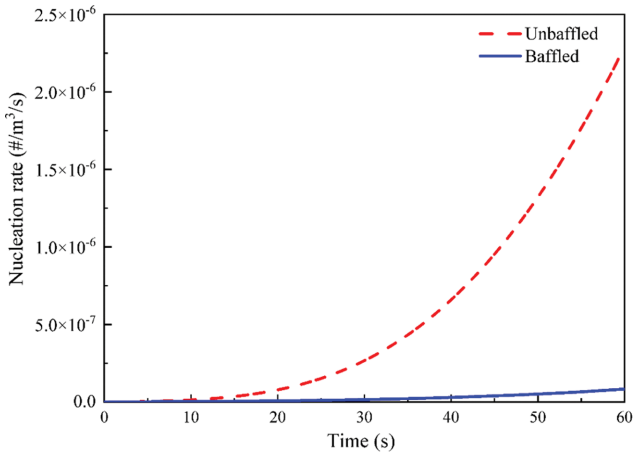

Fig. 10. Evolution of nucleation rate on the stirred vessel system.

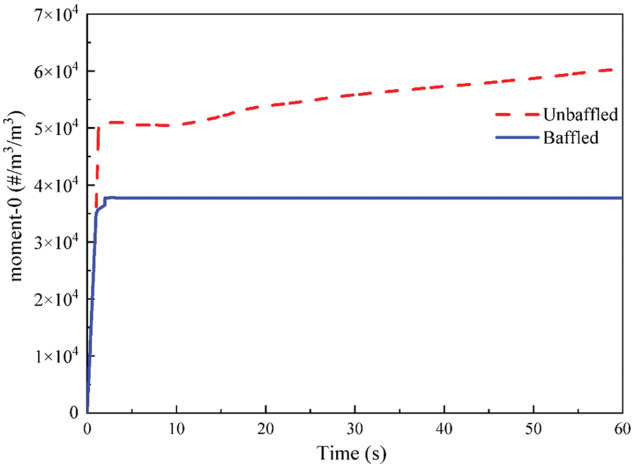

Fig. 11. Evolution of zeroth moment (m_0) in the stirred vessel systems.

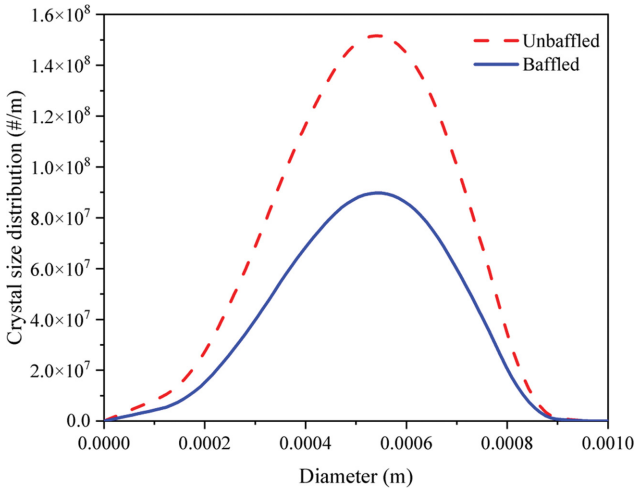

Fig. 12. Effect of the geometry of the system on crystal size distribution (CSD).

Further, the predicted nucleation rate is analyzed along y= −0.005 m. This is shown in Fig. 9. It is observed that the variation of the nucleation rate is found to be insignificant in the baffled stirred vessel system and significant for the unbaffled system. This is attributed to strong secondary recirculatory flow in the baffled stirred vessel. This is quantified and shown in Fig. 10 for the baffled and unbaffled stirred vessel. The rate of nucleation (volume-weighted average) increases exponentially with time in the unbaffled system due to the formation of small nuclei on the surface of the seed crystal. Hence, seed crystal growth rate would be at a slower rate. Thus, the expected yield of the crystals would be less in the unbaffled stirred vessel.

To quantify the crystallization process of KDP crystals, the predicted zeroth moment (total number of particles per unit volume of mixture suspension) is analyzed for the baffled and unbaffled system. This is shown in Fig. 11.

This characterizes the resistance due to the mass transfer of the solute to the number of seed crystals. In the baffled system, the zeroth moment value is observed to be constant. This indicates that the extent of nucleation is more insignificant than the growth of the crystals. However, in the unbaffled system, the magnitude of the zeroth moment is observed to be higher. This leads to a significant extent of nucleation and hence non-uniform product size in the unbaffled system. This is attributed to the formation of new crystals due to the higher nucleation rate. Thus, it affects the flowability of crystals in the unbaffled system, and longer batch times are required to obtain a higher yield in an unbaffled stirred vessel system. Here, the baffled system is found to be more advantageous to carry out the crystallization process.

The CSD determines the quality of the crystallization process. Here, seed particles (size: 500 μm) are introduced, and their effects on the CSD are analyzed for unbaffled and baffled stirred vessel configuration. This is shown in Fig. 12.

A significant difference in CSD is observed for unbaffled and baffled stirred vessel systems. The CSD is found to be narrow for the baffled system (area, 37752) and broader for the unbaffled system (area, 65214). The broader distribution in the unbaffled stirred vessel is attributed to the spatial inhomogeneity of supersaturation. The area under the curve indicates the number of crystals that are formed during the crystallization process. The number of crystals in the baffled system is found to be 42% lower than the unbaffled system. This indicates a more significant number of nucleated crystals in the unbaffled stirred vessel system, which is undesirable.

Table 1. Statistical reports of the unbaffled and baffled stirred vessel system

Stirred vessel type	Unbaffled	Baffled
De Brouckere mean diameter (d_{43}) (μm)	514	520
Number mean diameter (d_{10}) (μm)	513	516
B/G	4.61	0.25

This is further quantified by calculating statistical parameters such as De Brouckere mean diameter (d_{43}, moment-4/moment-3), coefficient of variation (COV), and number mean diameter (d_{10}, moment-1/moment-0) and are reported in Table 1.

It is observed that the magnitude of number mean diameter (d_{10}) and De Brouckere mean diameter (d_{43}) are higher for the baffled stirred vessel, indicating a higher growth rate. Since growth and nucleation rate is dependent on the supersaturation concentration, the ratio of nucleation (B) to the growth rate (G) is calculated. This is shown in Table 1. The value of B/G is found to be low for the baffled and high for the unbaffled stirred vessel systems. This is attributed to the significant growth of KH_2PO_4 crystals and insignificant nucleation in the baffled stirred vessel system. Thus, the baffled stirred vessel system is more advantageous to carry out the crystallization process, and hence further investigations are focused on the baffled stirred vessel.

4. Experimental Validation

The growth rate of KH_2PO_4 (KDP) crystals is calculated using Eq. (13) for various supersaturations. This is compared with the experimental data of Temmel et al. [21] and is shown in Fig. 13.

It is observed that the growth rate of KH_2PO_4 crystals increases linearly with supersaturation. The calculated error between numer-

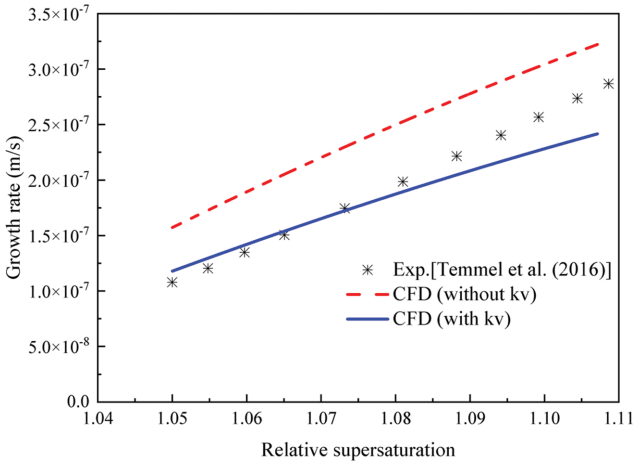

Fig. 13. Comparison of experimental data of growth rate and supersaturation with CFD predictions of the baffled stirred vessel.

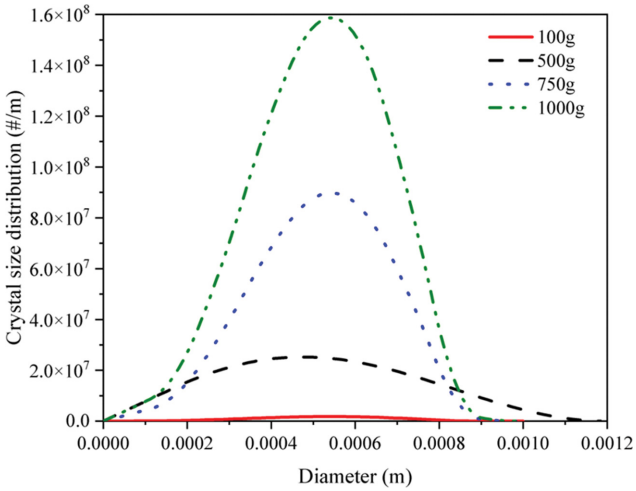

Fig. 14. Effect of different seed mass on the CSD.

ical and experimental data is found to be 25%, and it decreased to 7.5% by incorporating the volume shape factor (k_v=0.75) in the growth kinetics (Eq. (13)). Hence, the volume shape factor of crystals is found to be an essential parameter for the accurate prediction of crystal growth in the batch stirred vessel system [39].

5. Effect of amount, Size of Seed Crystals on CSD

To ensure narrow crystal size distribution with excellent flowability of crystals and to minimize the nucleation rate, seed crystals (KH_2PO_4) are introduced into the baffled stirred vessel system. However, limited information is available in the literature on the amount and size of seed crystals to be added that gives the desired CSD. Hence, different amount of seed crystals such as 100 g, 500 g, 750 g and 1,000 g with optimized size of 500 μm [45] are introduced into the system to find an optimum seeding loading that can improve a poorly behaved crystallization process. The predicted CSD for various amounts of seed crystals is shown in Fig. 14.

The narrow size distribution is observed when 750 g of seed crystals are used. This is quantified further by calculating the De Brouckere mean diameter (d_{43}) and mass of the seed crystals that are crystallized and is depicted in Table 2. The De Brouckere mean diameter (d_{43}) is observed to be high when 750 g of seed crystals are used. The crystallized mass increases with an increase in the number of seed crystals and decreases beyond 750 g. Hence, 750 g is considered to be a desirable amount of seed crystals that give a narrow distribution.

To analyze the effect of size of crystals on CSD, KH_2PO_4 seed crystals with different size range (100-700 μm) are introduced into the batch stirred vessel. The crystal size distribution is reconstructed from the moments and shown in Fig. 15.

The crystal size distribution is found to be broader when the seed crystal size is larger than 500 μm, and it is narrow when the

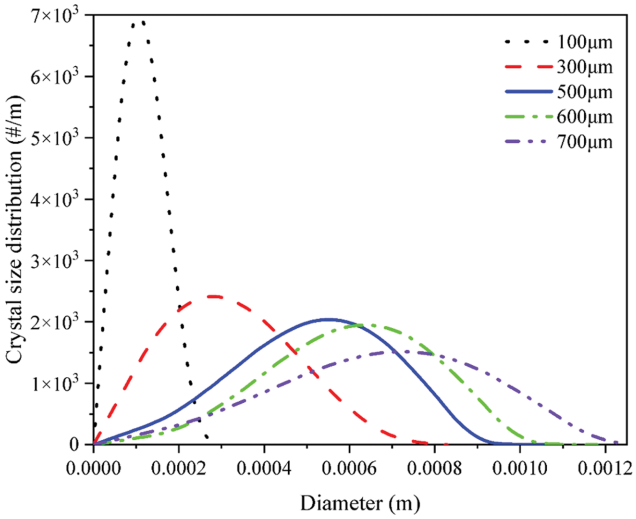

Fig. 15. Effect of seed crystal size on the normalized CSD.

seed crystal size is less than 500 μm. The broader crystal size distribution leads to a longer batch time for the crystallization process. This is quantified by calculating statistical parameters such as De Brouckere mean diameter (d_{43}), COV, and mass of the seed crystals that are crystallized, to quantify the crystal size distribution. This is reported in Table 3.

It is observed that the De Brouckere mean diameter (d_{43}) is smaller when seed crystals size is greater than 500 μm, which is considered the critical size. This occurs due to the formation of primary nucleation on the seed surface. Thus, De Brouckere mean diameter is found to be smaller. This is attributed to surface nucleation. The calculated coefficient of variation (COV) is observed to

Table 2. Effect of seed crystal amount on the mean size and crystallized mass

Seed mass (g)	100	500	750	1,000
De Brouckere mean diameter (d_{43}) (μm)	508	514	520	515
Crystallized mass (g)	0.0004	0.012	2.72	4.8

Table 3. Effect of seed crystal size on mean diameter, COV and crystallized mass

Seeding size (μm)	100	300	500	600	700
De Brouckere mean diameter (d_{43}) (μm)	140	330	520	550	660
COV	0.93	0.78	0.56	0.78	0.8
Crystallized mass (g)	0.13	0.73	2.72	5.19	10.63

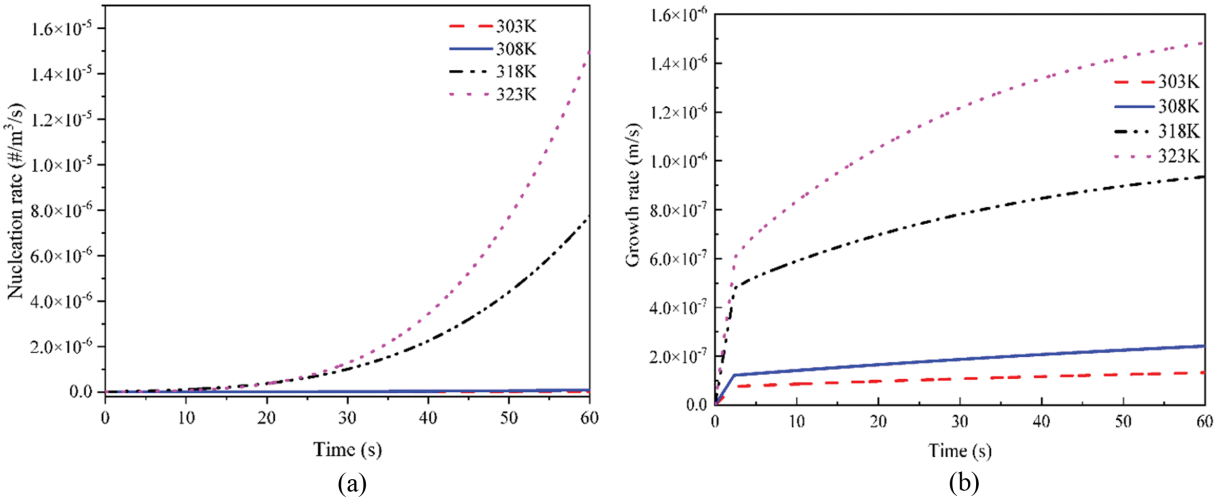

Fig. 16. Evolution of (a) nucleation and (b) growth rates for various seed crystal temperatures.

be minimum for 500 μm seed crystal size, and hence this size (500 μm) supports narrow size distribution. The calculated crystallized mass (Table 3) shows that its magnitude is considerably larger for seed crystal size greater than 500 μm. This is attributed to surface nucleation rather than growth. Hence, the smaller seed crystal size (<500 μm) supports narrow crystal size distribution (CSD) by suppressing primary nucleation.

6. Effect of Seed Crystal Temperature on Nucleation and Growth Rate

The effect of seeding temperature on the growth of KDP (KH_2PO_4) crystal is numerically analyzed for a wide range of temperatures (303-323 K) in the baffled stirred vessel. Here the solution temperature is maintained the same as the seed crystal temperature. The seed crystals are injected into the region between the metastable zone width and solubility curve (S=1.05) [21]. For various seeding temperature, solubility data are calculated using Temmel et al. [34]. The supersaturation is maintained at 1.05 so that the extent of nucleation is insignificant in our baffled stirred vessel. Here, walls of the stirred vessel are maintained at 298 K. The growth and nucleation rates are shown in Fig. 16(a)-(b).

It is found that the growth and nucleation rate increase linearly with an increase in the seeding temperature. Since the difference between seed crystal and wall temperature is related to the supersaturation, at higher seed crystal temperature (323 K), growth and nucleation rate are observed to be maximum. Also, at higher temperatures (323 K), both crystal growth and surface nucleation occur. To find a suitable temperature that supports the crystallization process, the ratio of nucleation over growth (B/G) is calculated. This is reported in Table 4. It is observed that its value is significantly larger when seed crystal temperature is greater than 308 K. When the ratio of B/G (nucleation/growth) is greater than 1 (i.e., T>308 K), uncontrolled nucleation occurs in the stirred vessel, which is undesirable, but when B/G is less than 1 (i.e., T<308 K) only crystal growth occurs (controlled nucleation).

Table 4. Effect of seeding temperature on nucleation (B)/growth (G)

Seeding temperature (K)	303	308	318	323
B/G	0.2	0.3	8.3	10.1

Hence, 308 K is considered as the optimum seeding temperature that supports crystal growth over nucleation. Hence it is advantageous to maintain a temperature difference of less than 10 K.

SUMMARY AND CONCLUSIONS

The flow field, mixing and crystal motion in a batch stirred vessel system was numerically investigated using CFD. The performance of the unbaffled stirred vessel was improved by incorporating a draft tube baffle. The spatial variation of velocity magnitude was analyzed to quantify the flow field. It was found that the recirculatory flow field prevails in the baffled stirred vessel system. The liquid circulation and predicted vorticity magnitude were analyzed for various rotational motion of the impeller, and optimum impeller speed (300 rpm) was identified. The effect of the flow field on the macro mixing was analyzed by injecting a buoyant tracer into the system. The mixing time was found to be less for the baffled stirred vessel system.

Further, the applicability of the stirred vessel system for crystallization of the KDP - water system was investigated. To predict the nucleation, growth and crystal size distribution (CSD) population

balance model (PBM) was used. The performance of the baffled stirred vessel was found to be superior over the unbaffled system. This is due to the significant extent of recirculatory flow and mixing among fluid elements in the baffled system. The crystal size distribution was found to be broader in the unbaffled system due to the higher nucleation rate. The significance of the volume shape factor (k_v) on crystal growth was analyzed and found to be an important parameter for the accurate prediction of crystal growth. Further, the effect of the amount of seed crystal and its size on CSD was studied. The crystal size distribution was found to be narrow when seed crystals of 750 g mass and 500 μm size were used. Hence, this seed mass and size is considered to be optimum. The effect of seed crystal temperature on nucleation and growth rate was analyzed. The performance of crystallization was found to be better at lower seed crystal temperature (308 K). Thus, nucleation, crystal growth and crystal size distribution of KH_2PO_4 are strongly dependent on local supersaturation, type of stirred vessel, seed amount and temperature distribution in a stirred vessel system.

Thus, hydrodynamics and fluid mixing strongly influence crystal growth (KH_2PO_4) in stirred vessel systems. Besides hydrodynamics and mixing, the quality of crystal size distribution (CSD) can be improved by a baffled stirred vessel system. Thus, this combined (CFD-PBM) approach helps understand the crystallization process in a batch stirred vessel system. The predicted results from this study could be important to assure efficient industrial operations of the batch crystallizer.

NOTES

The authors declare no competing financial interest.

NOMENCLATURE

C_{avg} : average concentration [kmol/L]
$c^*(\theta)$: equilibrium concentration of solute
COV : coefficient of variation
d_{43} : De Brouckere mean diameter [μm]
d_{10} : Number Mean diameter [μm]
k : turbulence kinetic energy [m^2/s^2]
m_0 : zeroth moment [$\#/m^3/m^3$]
N : speed of the impeller [s^{-1}]
t : time [s]
Ls : seed size [m]
G : growth rate [m/s]
B : nucleation rate [$\#/m^3 \cdot s$]
R : universal gas constant [J/mol·K]
S : relative supersaturation
T : temperature [K]
U : velocity [m/s]

Greek Letters

ρ : density of the fluid [kg/m^3]
ρ_c : density of the crystal [kg/m^3]
Γ : liquid circulation [m^2/s]
μ : viscosity of the fluid [Pa·s]
μ_i^s : moments
σ : standard deviation
ν : kinematic viscosity of the fluid [m^2/s]
θ : temperature [°C]

REFERENCES

1. Q. Su, Z. K. Nagy and C. D. Rielly, *Chem. Eng. Process. Process Intensif.*, **89**, 41 (2015).
2. Z. Gao, S. Rohani, J. Gong and J. Wang, *Engineering*, **3**, 343 (2017).
3. H. Ali and J. Solsvik, *Phys. Fluids*, **33**, 033319 (2021).
4. V. X. Mendoza-Escamilla, A. Alonzo-García, H. R. Mollinedo, I. González-Neria, J. Antonio Yáñez-Varela and S. A. Martinez-Delgadillo, *Chin. J. Chem. Eng.*, **26**, 942 (2018).
5. K. Steiros, P. J. K. Bruce, O. R. H. Buxton and J. C. Vassilicos, Springer Proc. in Phys., 363 (2016).
6. E. L. Paul, M. Midler and Y. Sun, *Handb. Ind. Mix.*, 1027 (2004).
7. S. Başbuğ, G. Papadakis and J. C. Vassilicos, *Phys. Rev. Fluids*, **3**, 084502 (2018).
8. H. S. Yoon, S. Balachandar and M. Y. Ha, *Phys. Fluids*, **21**, 085102 (2009).
9. K. Steiros, P. J. K. Bruce, O. R. H. Buxton and J. C. Vassilicos, *Phys. Rev. Fluids*, **2**, 094802 (2017).
10. J. F. Wendt, J. D. Anderson, J. Degroote, G. Degrez, E. Dick, R. Grundmann and J. Vierendeels, *Computational fluid dynamics: An introduction*, Springer Sci, & Business Media (2008).
11. X. Li, H. Zhao, Z. Zhang, Y. Liu and T. Zhang, *Chin. J. Chem. Eng.*, **29**, 57 (2021).
12. A. K. Pukkella, R. Vysyaraju, V. Tammishetti, B. Rai and S. Subramanian, *Chem. Eng. J.*, **358**, 621 (2019).
13. L. Wang, Y. Tian, Y. Qi, Y. Gao and M. Wang, *Particuology*, **56**, 91 (2021).
14. J. B. Joshi, N. K. Nere, C. V. Rane, B. N. Murthy, C. S. Mathpati, A. W. Patwardhan and V. V. Ranade, *Can. J. Chem. Eng.*, **89**, 754 (2011).
15. S. Vedantam and V. V. Ranade, *Sadhana - Acad. Proc. Eng. Sci.*, **38**, 1287 (2013).
16. S. Hara, S. Ebihara and Y. Kawaguchi, *Phys. Fluids*, **32**, 075102 (2020).
17. S. Sulttan and S. Rohani, *J. Cryst. Growth*, **505**, 19 (2019).
18. B. Szilágyi and Z. K. Nagy, *Cryst. Growth Des.*, **18**, 1415 (2018).
19. L. M. de Souza, E. Temmel, G. Janiga, A. Seidel-Morgenstern and D. Thévenin, *Chem. Eng. Sci.*, **232**, 116344 (2021).
20. S. Rohani, S. Horne and K. Murthy, *Org. Process Res. Dev.*, **9**, 858 (2005).
21. E. Temmel, M. Eicke, H. Lorenz and A. Seidel-Morgenstern, *Cryst. Growth Des.*, **16**, 6756 (2016).
22. D. Green, *Handb. Ind. Cryst.*, 181-199 (2002).
23. N. Doki, N. Kubota, A. Sato, M. Yokota, O. Hamada and F. Masumi, *AIChE J.*, **45**, 2527 (1999).
24. M. Lenka and D. Sarkar, *J. Cryst. Growth*, **486**, 130 (2018).
25. N. Doki, N. Kubota, M. Yokota and A. Chianese, *J. Chem. Eng. Japan*, **35**, 670 (2002).
26. M. Bohlin and Å. C. Rasmuson, *Can. J. Chem. Eng.*, **70**, 120 (1992).
27. N. Doki, N. Kubota, A. Sato and M. Yokota, *Chem. Eng. J.*, **81**, 313 (2001).

28. H. Wei, W. Zhou and J. Garside, *Ind. Eng. Chem. Res*., **40**, 5255 (2001).
29. Z. Wang, Z. Mao, C. Yang and X. Shen, *Chin. J. Chem. Eng*., **14**, 713 (2006).
30. M. Trampuž, D. Teslić and B. Likozar, *Chem. Eng. Res. Des*., **165**, 254 (2021).
31. D. A. Green, *Handb. Ind. Cryst*., 290-312 (2019).
32. T. Kumaresan and J. B. Joshi, *Chem. Eng. J*., **115**, 173 (2006).
33. B. Ashraf Ali, G. Janiga, E. Temmel, A. Seidel-Morgenstern and D. Thévenin, *J. Cryst. Growth*, **372**, 219 (2013).
34. E. Temmel, H. Eisenschmidt, H. Lorenz, K. Sundmacher and A. Seidel-Morgenstern, *Cryst. Growth Des*., **16**, 6743 (2016).
35. A. Lewis, M. Seckler, H. Kramer and G. Van Rosmalen, Industrial Crystallization: Fundamentals and Applications (Cambridge University Press, 2015).
36. D. Domínguez-Vázquez, G. B. Jacobs and D. M. Tartakovsky, *Phys. Fluids*, **33**, 033326 (2021).
37. C. Galletti, A. Paglianti, K. C. Lee and M. Yianneskis, *AIChE J*., **50**, 2050 (2004).
38. J. Ding and D. Gidaspow, *AIChE J*., **36**, 523 (1990).
39. A. Mersmann, *Crystallization technology handbook*, CRC press, Florida (2001).
40. R. McGraw, *Aerosol Sci. Technol*., **27**, 255 (1997).
41. K. Hemalatha and K. Y. Rani, *Ind. Eng. Chem. Res*., **56**, 6012 (2017).
42. V. John, I. Angelov, A. A. Öncül and D. Thévenin, *Chem. Eng. Sci*., **62**, 2890 (2007).
43. R. W. Fox, P. J. Pritchard and A. T. Mcdonald, *Introduction to fluid mechanics*, 7Th Ed., Wiley India Pvt. Limited (2009).
44. E. M. Marshall and A. Bakker, *Handb. Ind. Mix*., 257-353 (2001).
45. B. Ashraf Ali, M. Börner, M. Peglow, G. Janiga, A. Seidel-Morgenstern and D. Thévenin, *Cryst. Growth Des*., **15**, 145 (2015).